# An MSR1-Targeting Glycolipid Platform for Imaging the Changes of Phagocytic Macrophages in the Progression of Atherosclerotic Plaque

*Ming Zhai, Xiaomei Liu, Zhijun Lei, Qinyun Gu, Chendi Gao, Zi-Han Chen, Ya Zeng, Xiangyun Xu, Wei Wang, Bingyu Li, Yong Fan, Yefei Shi,* Guosong Chen,* and Wenhui Peng**

**The progression of atherosclerosis (AS) plaque is marked by a shift in the main cell component of phagocytic macrophages from myeloid-derived to vascular smooth muscle cell (VSMCs)-derived macrophages. It remains a great challenge to identify proper targeting markers and to image the changes of phagocytic macrophage, including myeloid-derived or VSMCs-derived macrophages. Herein, we propose macrophage scavenger receptor 1 (MSR1), as a detection marker of dynamic phagocytic macrophage changes in atherosclerotic plaques. To focus on this macrophage marker, we designed an MSR1-targeting synthetic glycolipid platform called sulfated L-fucopyranoside glycolipid (SFGL) SFGL is precisely fabricated based on a specially designed synthetic glycolipid with a well-defined structure, and it can be further co-assembled with functional components such as organic fluorescent molecules and inorganic gold nanoparticles to achieve multifunctionality. The study revealed the main cell component change of phagocytic macrophages from zsGreen positive ($\text{zsGreen}^{+}$) myeloid-derived $\text{MSR1}^{(\text{hi})}$ macrophages to tdTomato positive ($\text{tdTomato}^{+}$) VSMCs-derived $\text{MSR1}^{(\text{hi})}$ macrophages during AS progression in VSMCs lineage tracing atherosclerotic mice. This change indicates the progression of atherosclerotic plaque, as observed using Near-Infrared (NIR) imaging and micro-computed tomography (micro-CT). Based on the results, SFGL, with its exceptional targeting ability and convenient functionalization, is a promising candidate for both basic macrophage-tracking research and applications such as imaging and drug delivery.**

## 1. Introduction

Atherosclerosis is a clinically significant condition characterized by a complex interplay of cellular processes that contribute to the progression and instability of arterial plaques.[1–3] This condition often begins early in life and progresses with age, though the rate of progression varies unpredictably among individuals[4,5] Atherosclerosis typically remains asymptomatic for years or even decades, with clinical symptoms manifesting in later stages.[6] The accurate and reliable diagnosis of vulnerable atherosclerotic plaques before clinical manifestations is crucial for identifying high-risk patients and tailoring appropriate therapies.[7] As atherosclerosis develops, plaques undergo several pathological changes, including progression, rupture, and healing processes.[8] Current understanding attributes these pathological changes primarily to lipid accumulation and local inflammatory responses.[9] Various cell types participate in these pathological processes, including macrophages, vascular smooth muscle cells (VSMCs), lymphocytes, and neutrophils.[10]

---

M. Zhai, Z. Lei, W. Wang, Y. Shi, W. Peng
Department of Cardiology
Shanghai Tenth People's Hospital
School of Medicine
Tongji University
Shanghai 200070, China
E-mail: 1831183@tongji.edu.cn; pwenhui@tongji.edu.cn

X. Liu, C. Gao, Y. Zeng, X. Xu, G. Chen
The State Key Laboratory of Molecular Engineering of Polymers and Department of Macromolecular Science
Fudan University
Shanghai 200441, China
E-mail: guosong@fudan.edu.cn

The ORCID identification number(s) for the author(s) of this article can be found under https://doi.org/10.1002/adfm.202516172

**DOI: 10.1002/adfm.202516172**

Q. Gu, B. Li
School of Medicine
Tongji University
Shanghai 200092, China

B. Li
Zucker School of Medicine at Hofstra/Northwell
Lenox Hill Hospital
New York 10075, USA

Z.-H. Chen, Y. Fan
Department of Chemistry
Shanghai Key Laboratory of Molecular Catalysis and Innovative Materials and iChem
Fudan University
Shanghai 200441, China

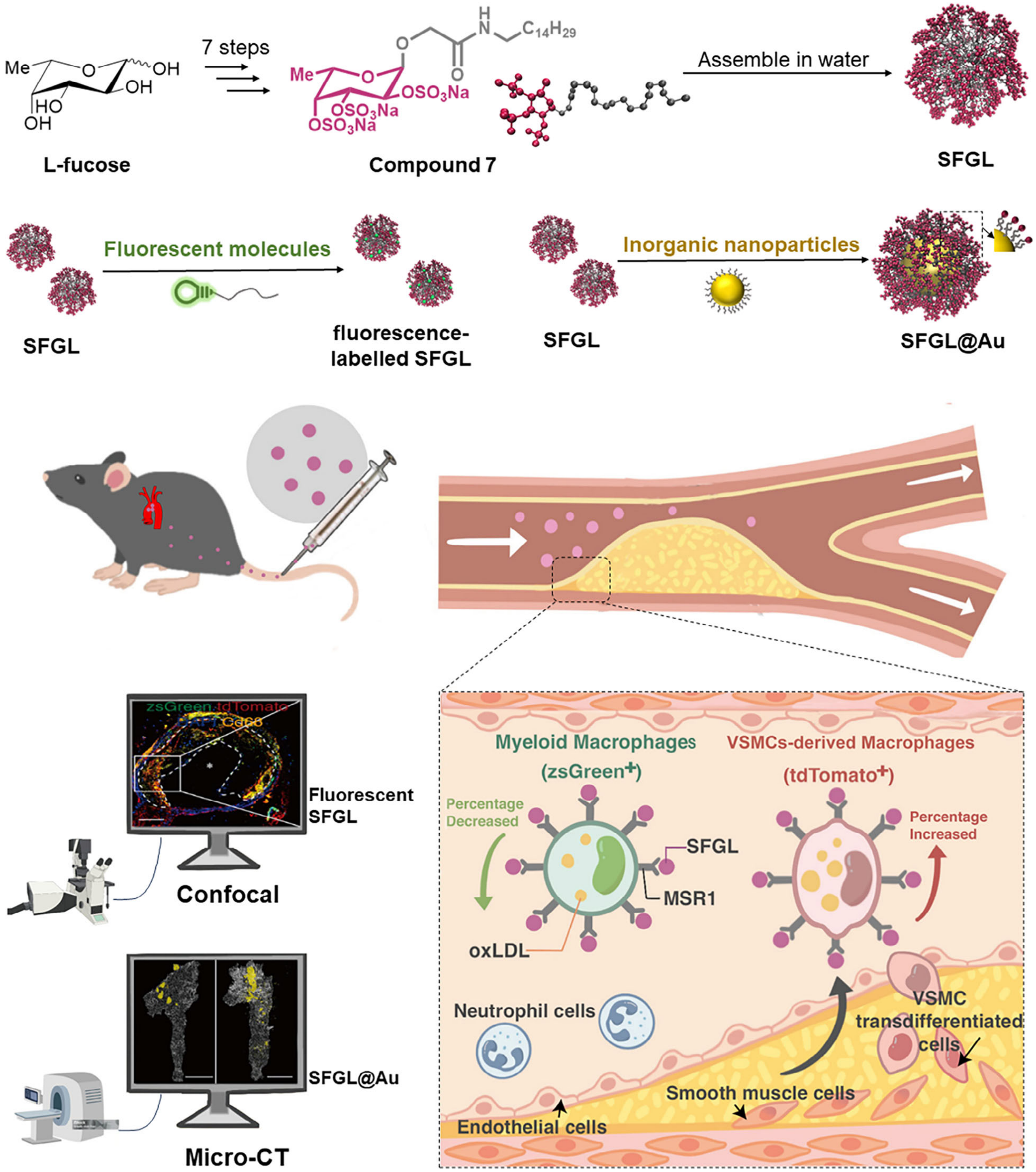

**Scheme 1.** Schematic diagram of the construction and targeting pathway of SFGL glycolipid platform.

Among these, the phagocytic macrophages play the most important role as mediators of inflammation and lipid accumulation in atherosclerosis environments by engulfing cellular debris and lipids.[11,12]

As atherosclerotic plaques progress, VSMCs proliferate, migrate into the intima, and transdifferentiate into phagocytic macrophages. These cells engulf lipids but process them less efficiently than myeloid-derived macrophages. This inefficiency leads to increased cell apoptosis, disintegration, and associated inflammatory responses, promoting plaque progression and vulnerability.[13–15] Furthermore, the significant presence of VSMC-derived phagocytic macrophages indicates the formation of advanced plaque.[16] Thus, atherosclerosis progression involves a shift in phagocytic macrophage origin, challenging to

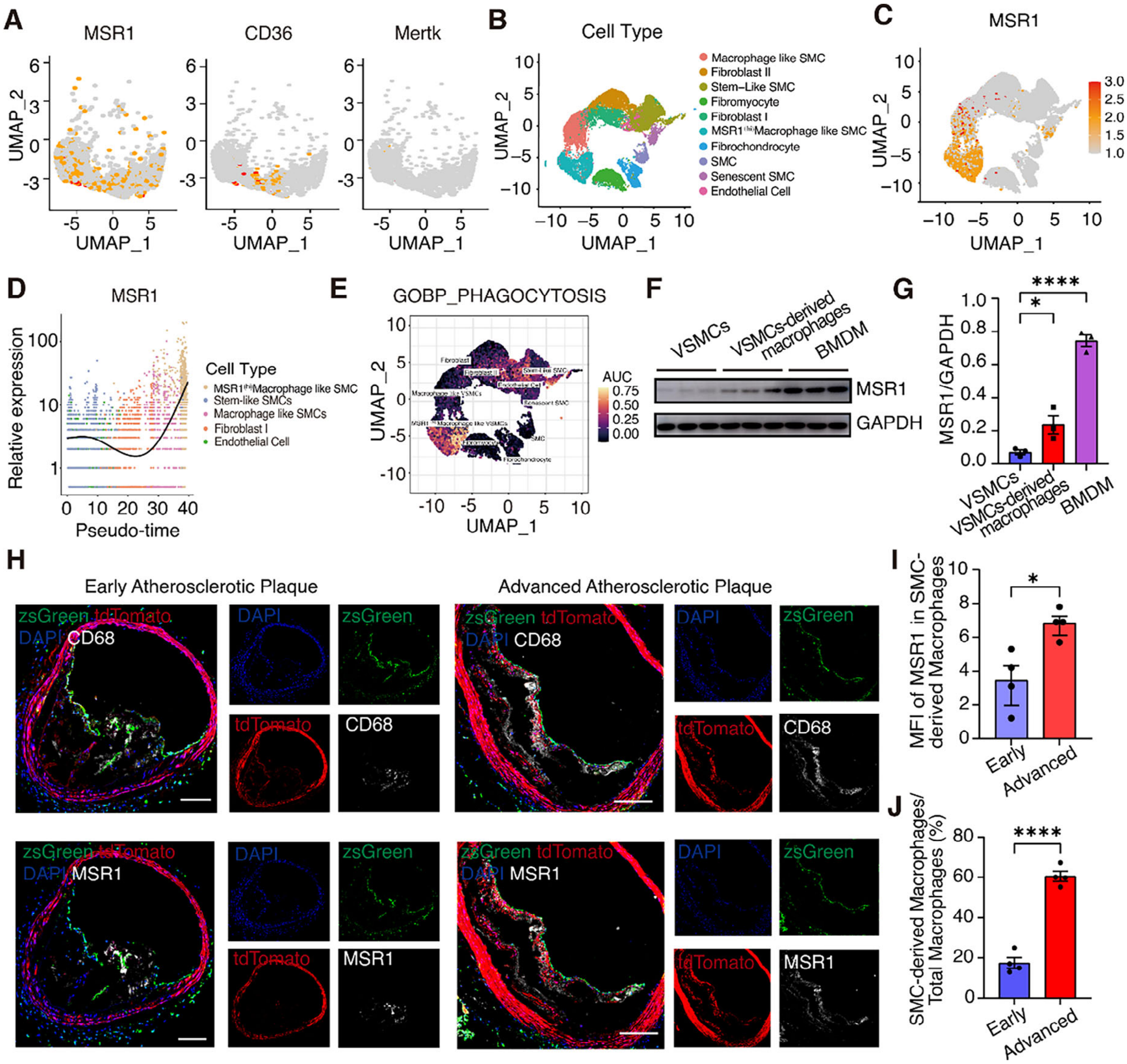

**Figure 1.** VSMCs-derived macrophages were activated into phagocytic MSR1$^{(hi)}$ VSMCs-derived macrophages in the process of atherosclerosis plaque development. A) Expression of different phagocytic genes in VSMCs-derived macrophages. B) Cell atlas of VSMCs-derived cells in GSE197073. C) Expression of MSR1 in different kinds of VSMCs-derived cells. D) The trajectory atlas of MSR1's expression change. E) Individual cell area-under-the-curve (AUC) values overlay for PHAGOCYTOSIS pathway activities. F) Protein expression level of MSR1 in VSMC, VSMCs-derived macrophages, and BMDM ($n = 3$ per group). G) Quantification of MSR1's expression in F ($n = 3$ per group). H) Representative images of immunofluorescence staining of CD68 and MSR1 in the adjacent series of early or advanced atherosclerotic plaque from VSMCs lineage tracing mice. Scale bar = 100 µm. ($n = 4$ per group). I) Quantification of mean fluorescence index (MFI) of MSR1 in VSMCs-derived macrophages in different stages of plaque. ($n = 4$ per group). J) Quantification of the percentage of VSMCs-derived macrophages in total macrophages (%) in different stages of plaque ($n = 4$ per group). Data were presented as mean ± SEM. $^{*}p < 0.05$, $^{****}p < 0.0001$. $p$-value was determined by one-way ANOVA with Bonferroni post-test (G) or unpaired two-tailed Student's $t$-test (I and J).

image dynamically. We propose SFGL as a complementary imaging platform to visualize these changes via lineage tracing, targeting MSR1.[17]

For invasive imaging, optical coherence tomography (OCT) can identify phagocytic macrophages during inflammatory activity, but has limited penetration for deeper VSMCs-derived macrophages.[18] Intravascular ultrasound (IVUS) imaging offers high penetration but is limited by resolution.[19] For non-invasive imaging, magnetic resonance imaging (MRI) is relatively slow and produces inconsistent image quality.[20] Compared with the IVUS and MRI, micro-computed tomography (micro-CT) enhanced with nanoparticles offers non-invasive operation and high-resolution images for identifying atherosclerotic plaque.[21,22] However, the micro-CT imaging method still cannot accurately capture the main phagocytic macrophages' component change, limiting its ability to precisely predict atherosclerotic plaque development.

Analysis of our previously published single-cell RNA sequencing (scRNA-seq) dataset revealed macrophage scavenger receptor 1 (MSR1), a macrophage scavenger receptor, as the highest expressed phagocytic gene in both VSMCs-derived and myeloid macrophages.[23] This finding suggested that designing a nanomaterial specifically targeting MSR1 could potentially enable monitoring of changes in both phagocytic macrophage populations. Furthermore, studies have shown that elevated MSR1 expression promotes atherosclerosis development, possibly by altering the response of macrophages to lipids or debris accumulated in the plaque.[24–26] Consequently, MSR1 emerges as a promising target for detecting both types of phagocytic macrophages and monitoring their main component changes during atherosclerotic plaque development.

Herein, we propose a novel MSR1-targeting platform based on synthetic glycolipids, called sulfated L-fucopyranoside glycolipid (SFGL), to detect main component changes in phagocytic macrophages during plaque progression and predict atherosclerotic plaque development via NIR imaging and micro-CT. SFGL is a supramolecular material assembled by specially designed synthetic glycolipids, consisting of sulfated L-fucopyranoside head and hydrophobic lipid tail (**Scheme 1**). The glycolipids are chemically synthesized from L-fucose through a seven-step process, resulting in a small molecule with a well-defined structure. The delicate hydrophilic-hydrophobic balance enables SFGL to form well-controlled nano-assemblies with an average diameter of 6 nm in aqueous solution. Furthermore, SFGL serves as a supramolecular scaffold supporting multifunctionality through dynamic coassembly with functional components. Multiple important imaging functions are achieved by combining SFGL with alkyl chain-modified fluorescent molecules for NIR imaging and inorganic nanoparticles for micro-CT.

Cell experiments verified SFGL's high targeting efficiency toward macrophages, including RAW264.7 and VSMCs-derived macrophages. Organ fluorescent images demonstrated that SFGL could precisely locate plaque in the aortic arch. Using a VSMC lineage tracing model, we proved that SFGL could reflect the main cell component changes of phagocytotic macrophages from myeloid (zsGreen$^+$MSR1$^+$) to VSMC-derived (tdTomato$^+$MSR1$^+$) as plaque progressed. In micro-CT imaging, SFGL@Au nanoparticles (Scheme 1) displayed increased CT signals in the aortic arch, indicating high specificity in recognizing and reflecting plaque pathological changes.

Our glycolipid supramolecular platform, SFGL, offered great advantages in efficient targeting, convenient functionalization, and easy preparation. These characteristics made SFGL a promising candidate for basic macrophage-targeting research and clinical applications in atherosclerosis as a new biomaterial.

## 2. Results

### 2.1. MSR1$^{(hi)}$ VSMCs-Derived Macrophages Gradually Increased, Leading to a Dominant Number of MSR1$^{(hi)}$ Macrophages in Advanced Plaque

Identifying highly expressed phagocytic genes offers potential avenues for targeting phagocytic cells, including myeloid and VSMCs-derived macrophages. We analyzed our previously published scRNA-seq dataset to find potential phagocytic genes highly expressed in both VSMC-derived and myeloid macrophages.[23] Our analysis revealed MSR1 was the highest-expressed phagocytic gene in VSMCs-derived macrophages (**Figure 1A**). Sub-clustering of tdTomato$^+$ cells uncovered a distinct group of VSMCs-derived macrophages with high MSR1 expression, which we termed MSR1$^{(hi)}$ VSMCs-derived macrophages (Figure 1B,C). Pseudo-time analysis demonstrated a gradual upregulation of MSR1 during VSMC to macrophage trans-differentiation (Figure 1D). Furthermore, GO enrichment analysis showed that MSR1$^{(hi)}$ VSMCs-derived macrophages marker genes were enriched in the "Phagocytosis" signaling pathway, which meant that the VSMCs-derived macrophages were activated into the phagocytic MSR1$^{(hi)}$ VSMCs-derived macrophages (Figure 1E).

To validate these findings experimentally, we used our previously published method to induce VSMCs' trans-differentiation into macrophages. We then examined MSR1 expression levels in VSMCs, VSMCs-derived macrophages, and myeloid-derived macrophages. Western blot analysis revealed increased MSR1 expression in VSMCs-derived macrophages compared to the control, confirming that cholesterol stimulation indeed promoted VSMCs to trans-differentiate into MSR1$^{(hi)}$ VSMCs-derived macrophages (Figure 1F,G). For comparison, the myeloid cells served as a positive control. We further conducted immunofluorescent staining for CD68 and MSR1 in early and advanced plaques. Our results demonstrated that the MSR1 staining positive area was larger in advanced plaques, which also exhibited a larger lipid core area, compared to early-stage plaques with smaller lipid cores. Furthermore, MSR1 expression in VSMCs-derived macrophages was significantly higher in advanced plaque than in their early counterparts (Figure 1H). Concurrently, we observed an increase in the number of VSMCs-derived macrophages highly expressing MSR1 (Figure 1I,J).

From these results, we concluded that as the plaque develops, the number of MSR1$^{(hi)}$ VSMCs-derived macrophages gradually increases, ultimately becoming the dominant macrophage population in advanced plaques.

### 2.2. Synthesis and Functionalization of SFGL

Given the high expression of MSR1 in VSMCs-derived macrophages, we designed a MSR1-targeting platform, SFGL, based on synthetic glycolipid amphiphiles. We selected sulfated L-fucopyranoside as the monosaccharide construct for these amphiphiles and serve as the targeting component. This choice was based on its role as the basic unit of fucoidan, a polysaccharide derived from brown algae and a known ligand of MSR1.[27,28] Meanwhile, the alkyl chains were designed to be linked via the anomeric functionalization of carbohydrates. The balance between the hydrophobicity of alkyl chains and hydrophilicity of carbohydrates induced self-assembly of the glycolipid in water, forming a targeting platform capable of incorporating other functional components such as organic small molecules and inorganic nanoparticles. This supramolecular design facilitated easy functionalization of SFGL through coassembly with alkyl chain-modified fluorescent molecules or inorganic nanoparticles. The synthesis of the glycolipid amphiphile from L-fucose was achieved through a seven-step process. Initially, L-fucose was peracetylated to obtain compound **1** (Figure S1, Supporting Information). The subsequent selective anomeric deprotection of the peracetylated L-fucose produced an anomeric hemiacetal, providing a single accessible hydroxyl group for further functionalization. This hemiacetal was alkylated with tert-butyl bromoacetate, resulting in compound **3** with a notable selectivity for the $\alpha$-anomer, and achieved in 75% yield. Following this, subsequent selective deprotection of the *tert*-butyl ester in compound **3** under acidic conditions was conducted using trifluoroacetic acid, and the corresponding free carboxylic acid **4** was obtained in high yield. Then, the free carboxylic acid **4** and 1-aminopentadecane were coupled into compound **5** via an amidation reaction. Acetyl groups on compound **5** were deprotected to give compound **6** with three available hydroxyl groups. Finally, the sulfated glycolipid amphiphile, compound **7**, was obtained through the total sulfation of hydroxyl groups in compound **6**. The detailed synthetic route is shown in Figure S1 (Supporting Information).

The self-assembly behaviors of SFGL in aqueous media was next explored. Upon dissolution in water, the synthetic glycolipid amphiphiles immediately formed nanoparticles with an average diameter of around 6 nm, as confirmed by cryo-TEM (**Figure** 2A). These nanoparticles exhibited a substantial negative zeta potential of -86.3 mV, attributed to the sulfated groups in glycolipids (Figure S3, Supporting Information).

In this way, we built up the MSR1-targeting platform SFGL, which featured hydrophobic cores composed of alkyl chains. This platform demonstrates remarkable versatility in incorporating various functional components through hydrophobic interaction, enabling further transfer to targeted positions. This functionality was demonstrated through the incorporation of organic small molecules and the integration of inorganic nanoparticles. We added FITC-C15, a fluorescein isothiocyanate (FITC) modified with an alkyl chain (Figure S1, Supporting Information), to the SFGL solution. The SFGL effectively captured these hydrophobic molecules in water, resulting in significantly higher fluorescence intensity compared to the system without SFGL. This enhanced fluorescence confirmed the successful combination of SFGL with FITC-C15 (Figure 2A). We applied the same method to incorporate gold nanoparticles decorated with alkyl chains into SFGL. As the results are shown in Figure 2A, initially, these gold nanoparticles were dispersed in chloroform. Upon addition of the SFGL aqueous solution, these gold nanoparticles were modified with SFGL and extracted into the upper water phase, which were named as SFGL@Au. This process resulted in a slight increase in gold nanoparticle size, consistent with a minor red shift observed in the UV spectrum (Figure S4A,B, Supporting Information). TEM imaging exhibited that the morphology of the gold nanoparticles remained similar before and after SFGL modification (Figure S4C,D, Supporting Information). The zeta potentials of the gold nanoparticle before and after conjugation with SFGL were also investigated. And the result showed that SFGL@Au had a higher negative charge (Figure S5, Supporting Information), indicating the modification of SFGL. The number of glycolipids modified on gold nanoparticles was roughly estimated. The results showed that $\approx$ 650 glycolipid molecules were conjugated to each gold nanoparticle, with the modification density of $\approx$1.44 molecules/nm$^2$. The exact calculation process was shown in Figure S6 (Supporting Information).

These results collectively demonstrated the SFGL platform's ability to easily incorporate both organic and inorganic functional components through a simple mixing process. The stability of SFGL was tested under different conditions (Figure S7, Supporting Information). SFGL showed the similar state in PBS and cell culture medium (DMEM with 10% FBS) with PDI of 0.37. And this platform exhibited good stability in cell culture medium within prolonged incubation time (10 days). SFGL showed no degradation after the addition of $H_2O_2$ and under NIR II light illumination. The stability of SFGL was also tested under varying pH levels, and it showed no change during this process (Figure S8, Supporting Information). Based on this platform, highly efficient targeting and tracing toward phagocytic macrophages during the process of atherosclerosis could be performed. Next, we explored the targeting ability of this platform both in vitro and in vivo.

### 2.3. The Targeting Ability of SFGL Toward MSR1$^{(hi)}$ Cells, Including MSR1$^{(hi)}$VSMCs-Derived Macrophages and MSR1$^{(hi)}$ Myeloid Macrophages, was Extensively Investigated both In Vitro and In Vivo

To elucidate the targeting efficacy of SFGL toward MSR1 on MSR1$^{(hi)}$ cells, we detected the ability of SFGL to bind to MSR1$^{(hi)}$ cells in vitro. We investigated its ability to bind to RAW264.7 and activated VSMCs-derived macrophages, as these cell types could express MSR1. So, we detected SFGL's targeting efficiency toward these two kinds of cells. First, the targeting ability of SFGL in vitro was investigated by confocal laser scanning microscopy in RAW264.7. After the RAW264.7 cells were incubated with SFGL at different concentration ranges from 10 to 100 µg mL$^{-1}$, the fluorescent intensity was found to be increased as the concentration rose (Figure 2B,C). We also assessed whether SFGL could influence the viability of these cells using the CCK-8 test, and our findings indicated that SFGL had minimal influence on cells' viability (Figure 2D). Quantitative assessment via flow cytometry showed that SFGL's targeting efficiency toward RAW264.7 cells (Figure 2E,F) reached optimal levels at 50 µg mL$^{-1}$, with no significant improvement at 100 µg mL$^{-1}$. This finding suggests an efficient targeting capability at moderate concentrations to detect the macrophages.

We utilized a myocardial infarction model to validate SFGL's target ability in vivo. Results showed that SFGL effectively targeted the MSR1$^{(hi)}$ cells in the infarcted area (Figure S9A,B, Supporting Information), demonstrating its potential for in vivo application. We then investigated SFGL's targeting efficiency toward VSMCs-derived macrophages. After the VSMCs were trans-differentiated into MSR1$^{(hi)}$ VSMCs-derived macrophages (Figure S10A,B, Supporting Information), we observed increased expression of macrophage-related marker genes and decreased expression of VSMC contractile marker genes (Figure S10C, Supporting Information). The Oil Red O staining confirmed the acquired ability of these cells to phagocytose lipid droplets, indicating successful transdifferentiation and activation into phagocytic macrophages in vitro.

For further investigation of SFGL's targeting specificity, we incubated both normal SMC and MSR1$^{(hi)}$ VSMCs-derived macrophages with varying concentrations of SFGL. We then assessed the targeting efficiency using flow cytometry. Our analysis revealed a significantly higher positive ratio for MSR1$^{(hi)}$ VSMCs-derived macrophages compared to normal SMCs when exposed

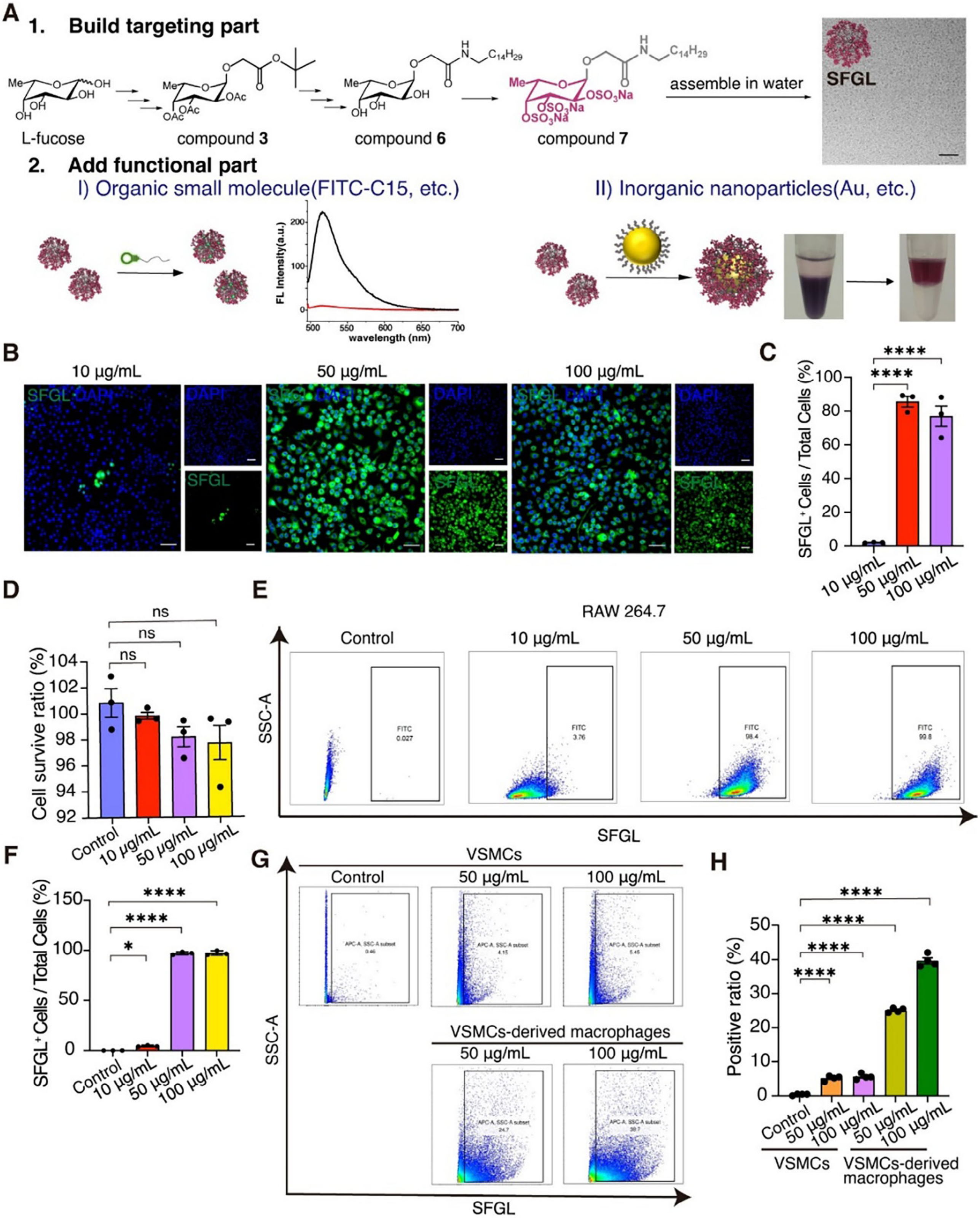

**Figure 2.** The construction of a targeting platform and the targeting ability of SFGL toward MSR1$^{(hi)}$ Cells, including MSR1$^{(hi)}$VSMCs-derived macrophages. A) Schematic diagram of the construction and functionality for SFGL targeting platform. There are two steps. In step 1, glycolipid SFGL was synthesized through the route shown above, and the targeting platform was built through directly dissolved SFGL in water. The cryo-TEM images showed the SFGL's assembly behavior. The scale bar is 50 nm. Step 2 was the addition of a functional part. After adding the fluorescent part, the SFGL

to the same SFGL concentration (Figure 2G,H). This marked difference in SFGL uptake between the two cell types demonstrates the SFGL's ability to specifically target MSR1$^{(hi)}$ cells, including MSR1$^{(hi)}$VSMCs-derived macrophages.

### 2.4. The Distribution of SFGL in Atherosclerotic Mice

Having established that a concentration of 50 μg mL$^{-1}$ SFGL achieved optimal macrophage targeting efficiency in vitro, we verified SFGL's targeting efficiency in vivo. we maintained this concentration in the mice plasma by injecting 0.69 μg kg$^{-1}$ SFGL into the tail vein of the subjects. The tracing distribution of SFGL was continuously observed using fluorescence imaging for 12 h post-intravenous injection of FITC-labeled SFGL. Atherosclerosis model mice exhibited distinct fluorescence signals in the arteries, while healthy mice showed no obvious fluorescence signal in the aorta (Figure S11A, Supporting Information).

To further characterize SFGL's distribution, we sacrificed mice at 3, 6, 12, and 24 h post-injection. Fluorescent analysis of the aorta and major organs (heart, liver, spleen, lung, and kidney) revealed a temporal trend in SFGL's localization. **Figure 3A,B** showed that the strongest fluorescent signals within the artery appeared 12 h post-injection, gradually attenuating thereafter. Notably, fluorescent signals in the aortic plaque reached their peak at 12 h and remained relatively stable through 24 h, with minimal decline (change in MFI $< 0.5$), suggesting sustained retention in the targeted pathological tissue. In contrast, SFGL signals in metabolic organs (e.g., liver and kidney) peaked earlier (liver at 6 h; kidney at 12 h) and then declined significantly (MFI decrease $> 1$), indicating active clearance. This accumulation in the liver may be related with negative surface charge of SFGL.[29] At the 24 h time point, the aorta exhibited the highest relative fluorescence intensity. This observation underscores SFGL's remarkable ability to target artery plaque, which was closely related with its saccharide part rather than negative charges.[30] The observed fluorescence kinetics across tissues, particularly the time-dependent decline in signal in liver and kidney, indicate that SFGL is cleared primarily via hepatic and renal pathways. The differential clearance rates and prolonged arterial retention provide indirect pharmacokinetic insights, consistent with the compound's design for targeting vascular activated phagocytic macrophages.

### 2.5. SFGL In Vivo Enables Imaging of Phagocytic Macrophage Change During Plaque Progression

Based on SFGL's ability to target MSR1, we sought to investigate SFGL's capacity to detect changes in the main component of phagocytic macrophages during plaque development. We injected the cy5-linked SFGL into VSMCs lineage tracing atherosclerotic mice. We then analyzed CD68 staining in series sections of early-stage and late-stage plaque from these mice. In early-stage atherosclerotic plaques, we found that SFGL-positive cells were predominantly enriched in the myeloid-derived macrophages region (zsGreen$^{+}$CD68$^{+}$), located on the plaque surface (**Figure 4A**). Conversely, in the late-stage plaques, the SFGL-positive cells were mainly concentrated in the VSMCs-derived macrophages region (tdTomaoto$^{+}$CD68$^{+}$), primarily situated at the atherosclerotic plaque's base (Figure 4B).

As the atherosclerotic plaques progressed, we observed an increase in the percentage of necrotic core (Figure 4C,D), indicating enhanced plaque vulnerability. Meanwhile, as the plaque progressed, we also noticed that the number of both myeloid-derived and VSMCs-derived macrophages increased (Figure 4E), with a corresponding rise in SFGL$^{+}$ cells of both lineages (Figure 4F). However, we noticed that the percentage of myeloid-derived macrophages among total macrophages decreased, while the percentage of VSMCs-derived macrophages increased (Figure S11B, Supporting Information). This trend was mirrored in the SFGL$^{+}$ cell population, with a decrease in the percentage of SFGL$^{+}$ myeloid-derived cells (from 55.42% to 26.51%) and an increase in SFGL$^{+}$ VSMCs-derived macrophages (from 44.58% to 73.49%).

These data demonstrated that the SFGL$^{+}$ cells accurately reflected the changing composition of phagocytic macrophage populations. These results indicated that the SFGL-identified cell component changes were mainly attributed to the main component of macrophages changed from myeloid macrophages to VSMCs-derived macrophages as plaque progressed.

### 2.6. SFGL's Targeting Ability Toward MSR1$^{(hi)}$ Cells Enables SFGL to Image the Phagocytic Macrophages Changes During Plaque Progression in Myh11$^{Cre}$B6G/R Lineage Tracing Mice

To examine the targeting efficacy of SFGL toward MSR1$^{(hi)}$ macrophages. By staining and imaging the MSR1 in the series of adjacent plaques slides of VSMC lineage tracing Ldlr$^{-/-}$ mice injected with SFGL, we found that the SFGL$^{+}$ area specifically colocalized with the MSR1$^{+}$ macrophage area. Meanwhile, we found that MSR1$^{+}$ and SFGL$^{+}$ cells showed synchronous increases during progression, demonstrating SFGL's in vivo target ability. (**Figure 5A,B**). Furthermore, to check the SFGL's ability to accurately image the phagocytic macrophages changes, we performed flow cytometry analysis using F4/80$^{+}$ CD204$^{(hi)}$ (MSR1$^{(hi)}$) as unique markers for detecting pathological phagocytic macrophages in Myh11$^{Cre}$ B6GR Ldlr$^{-/-}$ mice. Many reference papers used F4/80 and CD204$^{(hi)}$ (MSR1$^{(hi)}$) as unique markers in flow cytometry to distinguish the pathological macrophage sub-population.[31,32] We then used tdTomato$^{+}$

---

platform caught it and showed high fluorescence intensity. In the fluorescence spectrum, the black line represents the SFGL platform with fluorescent molecules, and the red line represents water with fluorescent molecules. For the imaging group, Au nanoparticles decorated with alkyl chains were transferred from the organic phase into the aqueous phase after adding SFGL. Au nanoparticles showed purple. B) Representative immunofluorescent images of SFGL combined positive RAW264.7 macrophages exposed to different concentrations of SFGL; Scale bar = 50 μm. C) Quantification of positive SFGL$^{+}$ cells / total cells in B, ($n = 3$ per group). D) CCK8 results of cell survival rate quantification. ($n = 3$ per group). E) Diagram of flow cytometry of RAW264.7 incubated with different concentrations of SFGL. F) Quantification of the SFGL$^{+}$ cells / total cells in the flow cytometry of E ($n = 3$ per group). G) Diagram of flow cytometry of SMC and CD68$^{+}$ SMC exposed to different concentrations of SFGL of 50 μg and 100 μg mL$^{-1}$, respectively. H) Quantification of the ratio of SFGL$^{+}$ cells in G, ($n = 4$ per group). Data were presented as mean ± SEM. $^{*}p < 0.05$, $^{****}p < 0.0001$, ns, no significance. $p$-value was determined by one-way ANOVA with Bonferroni post-test (C, E, G, H).

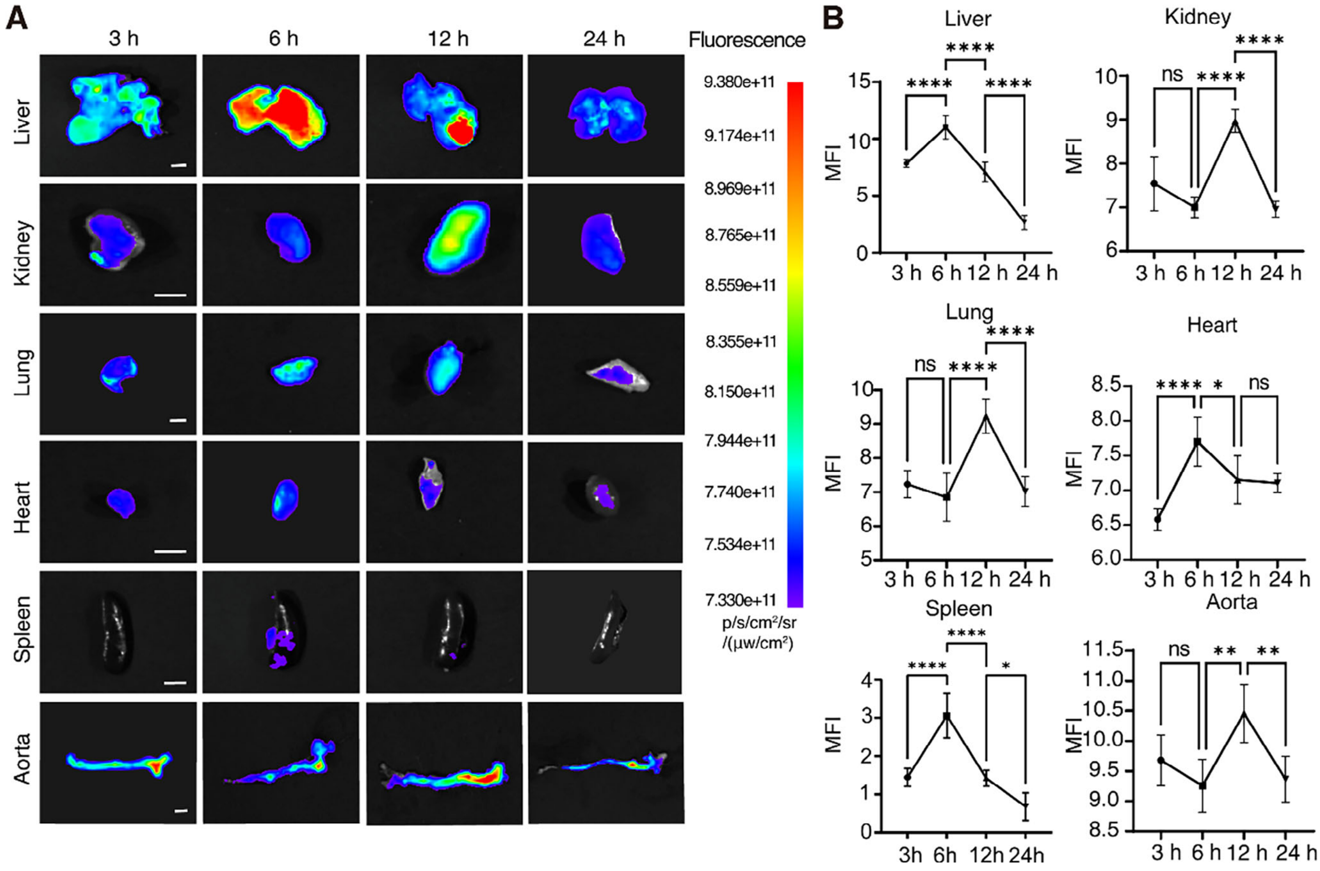

**Figure 3.** The tracing distribution of SFGL in atherosclerotic mice. A) Fluorescent representative imaging of different organs at different time points after SFGL's injection. Scale bar = 500 µm. B) Quantification of different organs' mean fluorescence index (MFI) of different organs at different time points after SFGL's injection. ($n = 3$ per group). Data were presented as mean ± SEM. $^*p < 0.05$, $^{**}p < 0.01$, $^{***}p < 0.001$, $^{****}p < 0.0001$, ns, no significant. $p$-value was determined by one-way ANOVA with Bonferroni post-test (C).

or zsGreen$^+$ signals to determine whether the cells were of VSMC origin or myeloid origin. Our results demonstrated that within SFGL$^+$F4/80$^+$ CD204$^{(hi)}$ (MSR1$^{(hi)}$) cells, early plaques showed predominant zsGreen$^+$ signal (myeloid-derived), while late plaques exhibited increased tdTomato$^+$ population (VSMC-derived). Quantitative analysis revealed a significant ($p < 0.01$) shift in phagocytic macrophage origin within SFGL$^+$F4/80$^+$ CD204$^{(hi)}$ (MSR1$^{(hi)}$) cells: myeloid-derived (zsGreen$^+$) populations dominated early plaques (72.3%), while smooth muscle cell-derived (tdTomato$^+$) populations predominated in advanced lesions (72.9%) (Figure 5C,D). These findings provided direct evidence of SFGL's ability to image the phagocytic changes during plaque progression.

### 2.7. SFGL's Targeting Ability Toward MSR1$^{(hi)}$ Cells Enables SFGL to Image the Phagocytic Macrophages Changes During Plaque Progression in Myh11$^{Cre}$ B6G/R Lineage Tracing Mice

### 2.8. SFGL Enables Triple-Modal Micro-CT/NIR-II/PA Imaging for Precise Tracking of Atherosclerotic Plaque Progression

Considering plasmonic gold nanoparticles were widely used in micro-CT imaging due to their excellent biocompatibility and imaging capabilities,[33] we developed SFGL@Au by linking SFGL with gold nanoparticles to enable micro-CT detection of SFGL. A micro-CT imaging platform was used to visualize plaques following SFGL@Au injection. As a negative control, we administered gold nanoparticles alone, which yielded no significant enhanced signals within the atherosclerotic plaque in arteries harvested from the high-fat diet (HFD)-fed atherosclerotic mice. In contrast, SFGL@Au markedly enhanced the micro-CT signals of the artery plaques in the *Ldlr*$^{-/-}$ mice (Figure S11C,D, Supporting Information).

Considering SFGL could detect the activated phagocytic MSR1$^{(hi)}$ VSMCs-derived macrophages in atherosclerosis plaque, we explored its potential application in monitoring plaque progression. Our previous data indicated that the increasing trend of phagocytic MSR1$^{(hi)}$VSMCs-derived macrophages could reflect changes in atherosclerotic plaque size in vivo. Consequently, we investigated whether SFGL@Au could capture the plaque progression under micro-CT imaging. We injected the SFGL@Au into atherosclerotic mice fed with either short-term or long-term HFD. Our findings revealed that in the advanced plaques, the area positive for SFGL identified by CT was significantly larger than in early-stage plaque (**Figure 6**A,B).

To validate the correlation, we performed a histological analysis of the harvested artery plaques and compared the results with

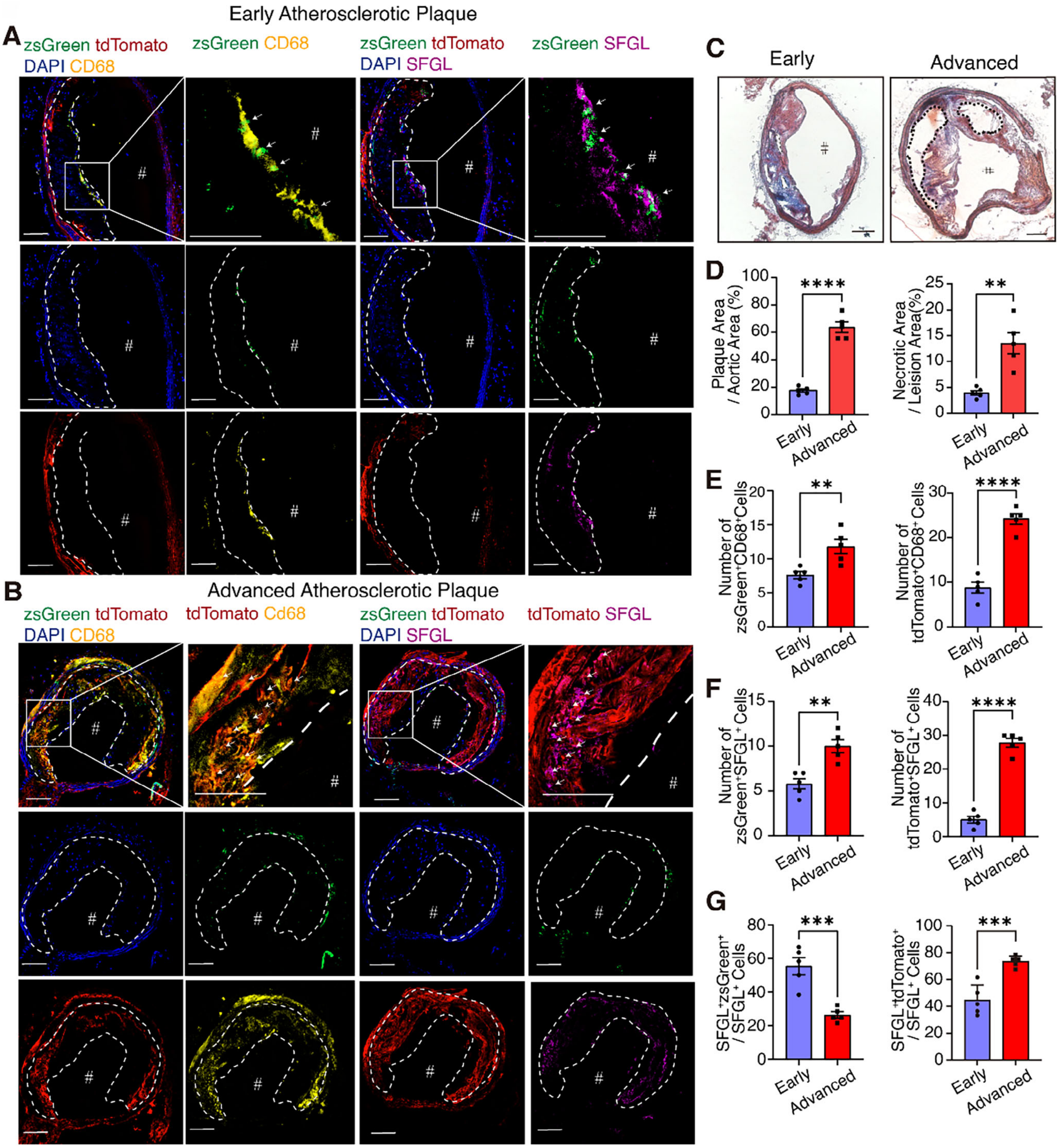

**Figure 4.** SFGL's in vivo targeted imaging of vulnerable plaques in VSMCs lineage tracing mice. A) Regions of early stages adjacent series sections of atherosclerotic plaque had macrophages (CD68$^+$) co-localized with SFGL$^+$ cells. Scale bar = 100 µm. B) Regions of advanced-stage adjacent series sections of atherosclerotic plaque had macrophages (CD68$^+$) co-localized with SFGL$^+$ cells. Scale bar = 100 µm. C) Masson staining representative images of the plaque in A & B. Scale bar = 100 µm. D) Quantification of plaque area percentage of A & B (left). Quantification of necrosis area percentage of plaque in C (right). ($n = 5$ per group). E) Quantification of the number of zsGreen$^+$CD68$^+$ and tdTomato$^+$CD68$^+$ cells in early-stage and advanced-stage atherosclerotic plaque. ($n = 5$ per group). F) Number of zsGreen$^+$ SFGL$^+$ cells in early-stage and advanced-stage atherosclerotic plaque. ($n = 5$ per group). G) Percentage of zsGreen$^+$ SFGL$^+$ cells and tdTomato$^+$ SFGL$^+$ cells of SFGL$^+$ cells, respectively. ($n = 5$ per group). Data were presented as mean ± SEM. $^{**}p < 0.01$, $^{***}p<0.001$, $^{****}p < 0.0001$. $p$-value was determined by unpaired two-tailed Student's $t$-test. The white dotted line indicated plaque area. The white # indicated the lumen area within the plaque.

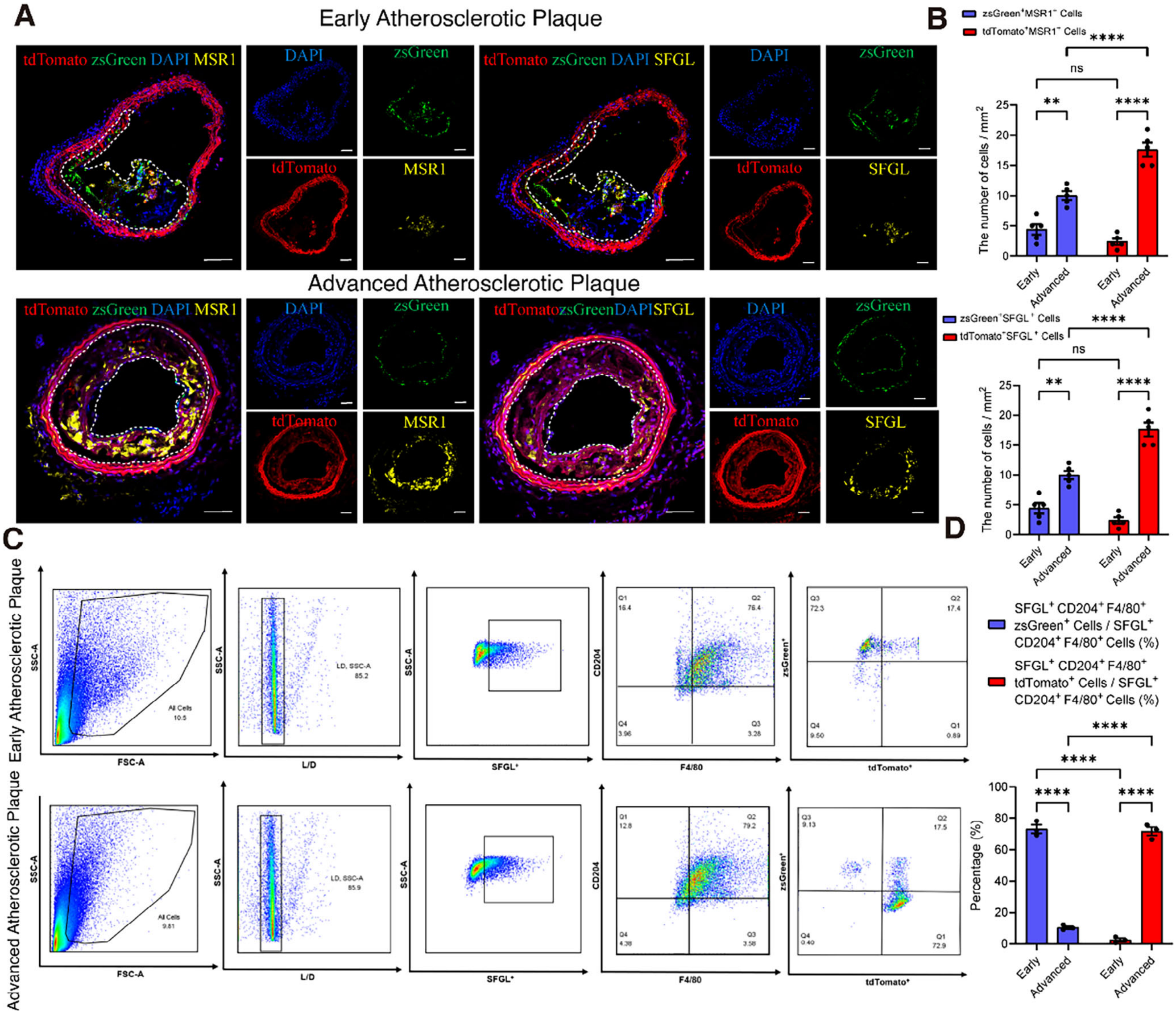

**Figure 5.** A) Regions of early and late stages, adjacent series sections of atherosclerotic plaque, CD68$^+$ co-localized with SFGL$^+$ cells. Scale bar = 100 µm. B) Quantification of the number of zsGreen$^+$MSR1$^+$ and tdTomato$^+$MSR1$^+$ cells in early-stage and advanced-stage atherosclerotic plaque. (down). Quantification of the number of zsGreen$^+$SFGL$^+$ and tdTomato$^+$SFGL$^+$ cells in early-stage and advanced-stage atherosclerotic plaque. ($n = 5$ per group). C) Diagram of flow cytometry of SFGL$^+$ CD204$^+$ F4/80$^+$ zsGreen$^+$ cells and SFGL$^+$ CD204$^+$ F4/80$^+$ tdTomato$^+$ cells changed in the process of atherosclerosis plaque progression. D) Quantification of the SFGL$^+$ CD204$^+$ F4/80$^+$ tdTomato$^+$ cells or SFGL$^+$ CD204$^+$ F4/80$^+$ zsGreen$^+$ cells / SFGL$^+$ CD204$^+$ F4/80$^+$ in the flow cytometry of C. ($n = 5$ per group). Data were presented as mean ± SEM. $^{**}p < 0.01$, $^{****}p < 0.0001$. $P$-value was determined by an unpaired two-tailed Student's $t$-test.

SFGL@Au micro-CT imaging. We found a positive correlation between plaque size and the area of SFGL@Au accumulation under micro-CT imaging (Figure 6C). Our findings demonstrated that as plaque volume increased (as evidenced by micro-CT results), there was a corresponding decrease in collagen content (Col3a1-positive areas) alongside an increase in instability markers (MMP9-positive areas). These observations indicated that plaque instability progresses with plaque development, which was consistent with the SFGL@Au-based detection of plaque progression. (Figure 6D–F). Building upon the established micro-CT imaging capabilities of plasmonic gold nanoparticles, we developed SFGL@Au by co-conjugating SFGL with both gold nanoparticles and NIR-II fluorophores IR1061 (emission >1000 nm) for dual-modal imaging. In vivo NIR-II imaging revealed strong, specific signals (SBR = 5.2) at aorta plaque lesions in the SFGL injected group, but there was no signal at all in the PBS group, both groups' aortic plaque could be stained. (Figure 6G; Figure S11E, Supporting Information), while co-localized micro-CT contrast confirmed targeted accumulation in aorta plaque lesions (Figure S11F, Supporting Information). The NIR-II component enabled real-time tracking of plaque development in living animals, while micro-CT provided high-resolution anatomical localization, together establishing SFGL@Au as a comprehensive imaging platform for atherosclerosis monitoring.

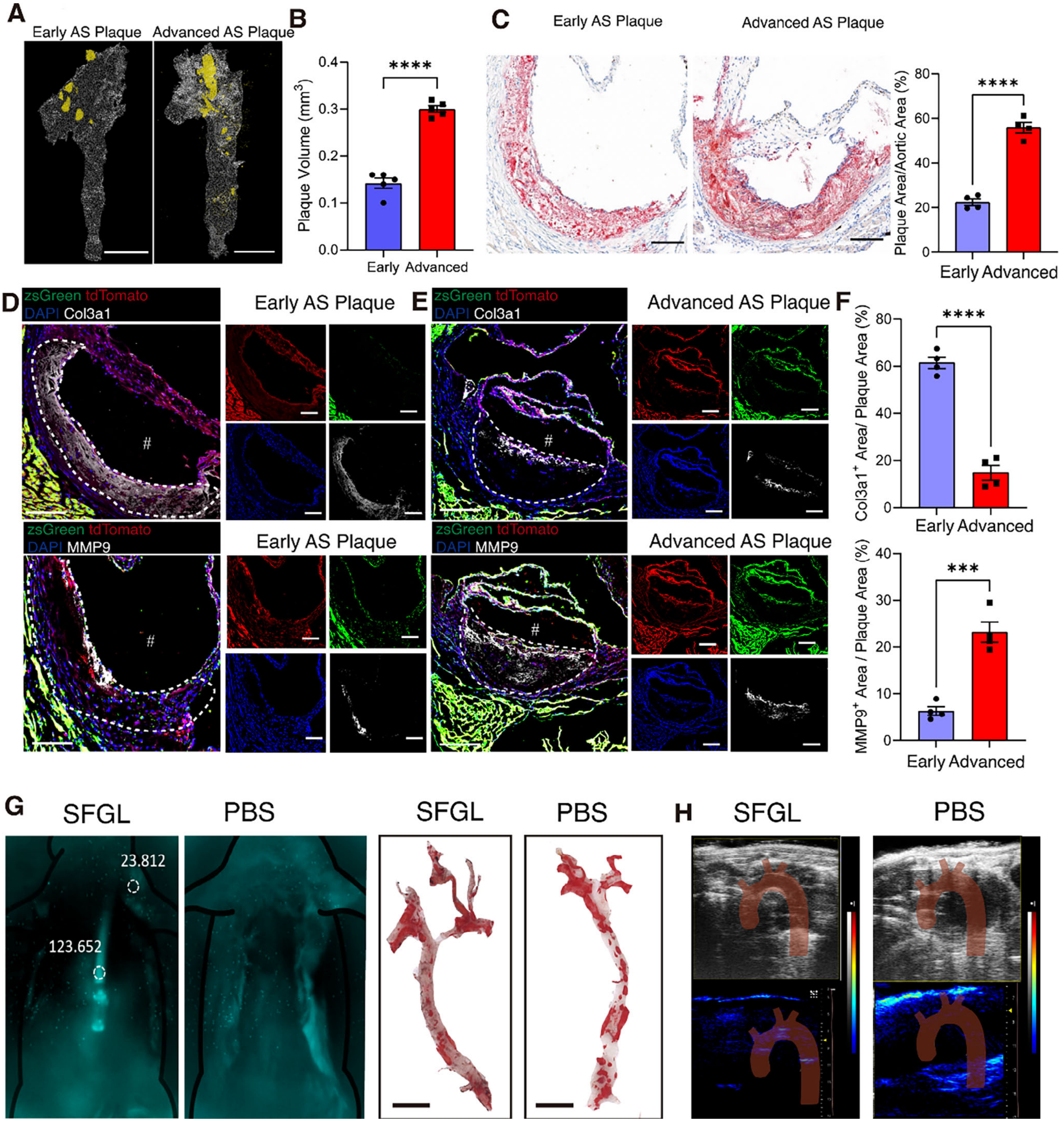

**Figure 6.** MSR1-targeted SFGL can image the vulnerable plaque progression under micro-CT A) CT images of the aorta with early or advanced atherosclerotic plaque from mice after injected with gold conjugated SFGL. Scale bar = 500 µm. ($n = 5$ per group). B) Quantification of plaque volume in A. C) Representative Oil Red O staining images of plaque and quantification of the ratio of lesion Area / Lumen Area ratio. ($n = 4$ per group). D) the representative IF images of Colea1 and MMP9 staining in 16w plaque series slides. E) the representative IF images of Colea1 and MMP9 staining in 24w plaque series slides. F) the quantification of Col3a1$^{+}$ area or MMP9$^{+}$ area change as the plaque progressed. ($n = 4$ per group). G) the representative NIR images show that the SFGL can enhance the atherosclerotic aortic plaque in vivo. SBR = 5.2. ($n = 3$ per group). H) the representative PA images show that the SFGL can enhance the atherosclerotic plaque in the aortic arch in vivo. ($n = 4$ per group). Scale bar = 20 µm. Data were presented as mean ± SEM. ****$p < 0.0001$. $P$-value was determined by unpaired two-tailed Student's $t$-test.

Furthermore, to further expand SFGL's in vivo atherosclerosis ability, we conducted complementary photoacoustic (PA) imaging using SFGL-Cy5 conjugates, and we found that strong PA signal intensity at aortic arch plaques increased; however, the control group's PA signal intensity was negative. (Figure 6H) To further validate SFGL@Au's distribution, we quantified gold concentration in various organs, feces, and urine after 24 h post-injection by using ICP-OES. The quantitative analysis of gold content (%) showed significantly higher accumulation in aortic atherosclerotic lesions (10%) compared to non-target tissues ($<6\%$, $p<0.01$), while ICP-MS revealed elevated AuNP levels in urine and feces at 24 h, confirming renal and hepatobiliary clearance as the primary elimination routes. The agreement between fluorescence imaging and ICP-MS validated the biodistribution data, collectively demonstrating SFGL@Au's preferential targeting of plaques and its progressive clearance via excretory pathways. These findings provided a comprehensive pharmacokinetic profile of SFGL@Au, highlighting both its selective plaque accumulation and efficient systemic elimination. (Figure S12A, Supporting Information). This observation was consistent with our previous in vivo NIR fluorescence imaging data, reinforcing SFGL@Au's high affinity for atherosclerosis plaques in aortas. The Excretion Rate of SFGL@Au was calculated through the following equation: (Au content detected in excretions)/ Total injected dose * 100%, we found that the Excretion Rate of SFGL@Au was 49.33%. Furthermore, we found that the gold content in urine (43.04%) is significantly higher than that in feces (6.290%), this indicated that the SFGL@Au mainly excreted by kidney and urine. These micro-CT imaging results clearly illustrated that SFGL@Au could selectively accumulate in the atherosclerotic plaque lesion. Furthermore, we scanned the livers and spleens from SFGL@Au injected mice. Notably, no obvious signals were detected in these organs under micro-CT, further confirming SFGL@Au's strong affinity for atherosclerotic plaque (Figure S12B, Supporting Information). These results suggested that the SFGL@Au could serve as an enhanced imaging method under micro-CT to identify and quantify increasing populations of phagocytic MSR1$^{(hi)}$VSMCs-derived macrophages.

## 3. Conclusion

We have introduced an innovative targeting platform, SFGL, designed to track the dynamic shift in phagocytic macrophage populations during atherosclerotic plaque development. This platform capitalized MSR1 as a key target, exploiting its high expression in both phagocytic and myeloid macrophages. The SFGL platform, as supramolecular materials assembled from glycolipid amphiphiles in aqueous solutions, enabled precise identification and imaging of phagocytic cells within plaque lesions, facilitating detailed analysis of their distribution and temporal changes.

We proved the MSR1-targeting capability of SFGL, which precisely tracked the phagocytic macrophage origin and phenotypic switching during plaque progression. This was demonstrated by flow cytometry. Flow cytometry analysis of F4/80$^{+}$CD204$^{(hi)}$ populations revealed a significant ($_{p}$ < 0.01) transition from myeloid-derived (72.3% zsGreen$^{+}$) to VSMCs-derived (72.9% tdTomato$^{+}$) macrophages between early and advanced plaques, respectively. These findings established SFGL as an effective tool for monitoring macrophage origin dynamics change in atherosclerosis. The quantitative correlation between MSR1 expression and SFGL accumulation further validated its targeting specificity for pathological phagocytic macrophages.

Traditional imaging modalities, such as CT and MRI, often lacked the resolution to capture cellular and molecular changes within plaques. Although the main phagocytic macrophage component change from myeloid macrophages to VSMCs-derived macrophages was an important indicator of vulnerable plaque formation, previous attempts using macrophage-specific nanoparticles for CT or MRI imaging have overlooked the importance of monitoring this phagocytic macrophage component change for accurate plaque assessment.[32] SFGL addressed this limitation by specifically targeting and tracking these cellular transitions, offering a more precise evaluation of plaque development. Our results further demonstrated that SFGL, when combined with gold nanoparticles (SFGL@Au), could accurately visualize atherosclerotic plaque progression under micro-CT imaging, correlating well with histological findings. Notably, only 50 μg of SFGL@Au per mouse was required for effective imaging, which was a significantly lower dose compared to conventional CT contrast agents. This reduction in required dosage minimizes potential toxicity, enhancing SFGL's clinical potential. Furthermore, unlike polysaccharide-based biomaterials with uncertain constituents,[31,34] SFGL was constructed by glycolipids with a precise chemical structure, which facilitated its functional reproducibility and reliability. The modular design of SFGL, based on supramolecular interaction, also allowed facile combination with diverse contrast agents, thereby enabling multimodal imaging capabilities.

Overall, SFGL represented a significant advancement in imaging technology for atherosclerosis, combining high targeting affinity, precise component detection, convenient functionalization, and precise chemical structure. Its ability to track changes in phagocytic macrophages, provided valuable insights into plaque development, making SFGL a promising candidate for clinical applications in the diagnosis and treatment of atherosclerosis.

## 4. Experimental Section

Materials and the exact synthetic routes are documented in the Supporting Information.

*Fabrication of MSR1-Targeting Platform SFGL*: The SFGL platform was constructed by dissolving compound **7** in water at a 5 mg mL$^{-1}$ concentration under vigorous stirring. The SFGL aqueous solution had a strong Tyndall effect, which indicated the self-assembly of glycolipids.

*Fabrication of Fluorescence-Labeled SFGL*: To create the fluorescent-labelled SFGL, we first linked fluorescent molecules with hydrophobic alkyl chains. In this way, these decorated dye molecules gathered aggregated in water and showed little fluorescence intensity because of aggregation-caused quenching. However, upon adding these fluorescence groups to SFGL aqueous solution with a mass ratio of 1%, we observed the fluorescence intensity immediately increased a lot, which indicated the successful assembly of SFGL with fluorescence molecules (Figure 2A).

*Fabrication of Gold Nanoparticles Decorated with SFGL*: First, gold nanoparticles with an average diameter of 12 nm were fabricated in water by mixing 2.4 mL of 10 mM $HAuCl_4$ and 3 mL of 0.1 M sodium citrate under vigorous stirring. Then these gold nanoparticles were prefunctionalized with alkyl chains and dispersed in $CHCl_3$ through a two-step ligand exchange approach using n-dodecanethiol (n-$C_{12}H_{25}SH$).[35,36] Typically, 0.4 mL of the concentrated (≈0.8 mg mL$^{-1}$) aqueous solution of gold nanoparticles was added to 10 mL of 19.3 μL n-$C_{12}H_{25}SH$ in DMF.

The solution was sonicated for 30 min and incubated overnight. The modified gold nanoparticles were washed with $CHCl_3$ three times and concentrated. Subsequently, these concentrated gold nanoparticles were added into 10 mL of 19.3 µL n-$C_{12}H_{25}SH$ in $CHCl_3$. Followed by the same sonication, incubation, and purification process, we finally obtained gold nanoparticles modified with alkyl chains (C12H25-) in $CHCl_3$. Through simply mixing SFGL aqueous solution with gold nanoparticles suspended in $CHCl_3$, the glycolipid SFGL was absorbed onto the surface of gold nanoparticles through virtue of hydrophobic interaction. In this way, the gold nanoparticles were transferred into water, and SFGL@Au was successfully fabricated (Figure 2A; Figure S4, Supporting Information). The transmission electron microscopy (TEM) images showed that SFGL@Au nanoparticles maintained an average diameter of 12 nm (Figure S4C,D, Supporting Information). However, the dynamic light scattering results showed that the hydrodynamic diameter of SFGL@Au was around 25 nm, which might be due to the negative charged surface of SFGL. Besides, the result also showed that SFGL@Au had a narrow distribution with polydispersity index of 0.3 (Figure S4B, Supporting Information).

*Fabrication of SFGL with Fluorescent Molecules and Gold Nanoparticles*: The gold nanoparticles combined with SFGL through the method mentioned above. Then fluorescent molecules were added into the system with the mass ratio of 1% under sonication. In this way, SFGL could combine with different agents to realize multiple imaging methods.

*Animals*: In our study, we crossed the **Myh11$^{\text{Cre}}$** mice (a genetically engineered mouse model in which the **Cre recombinase** gene was inserted under the control of the **Myh11** promoter) with **CAG-LoxP-ZsGreen-Stop-LoxP-Tdtomato (B6-G/R) Ldlr$^{-/-}$** mice to generate the **Myh11$^{\text{Cre}}$ B6-G/R Ldlr$^{-/-}$ SMCs lineage-tracing mice atherosclerotic model** to investigate. Following tamoxifen induction, the **zsGreen reporter** was excised in SMCs only due to high **Myh11$^{\text{Cre}}$ recombinase expression** in SMCs, resulting in **tdTomato** expression. In contrast, myeloid cells retained zsGreen fluorescence because of their negligible Myh11$^{\text{Cre}}$ expression. This allowed us to distinguish SMCs (tdTomato$^{+)}$ from myeloid cells (zsGreen$^{+}$) based on their distinct fluorescent reporter profiles. At 8-week of age, these mice were intraperitoneally injected with 75 mg k$^{-1}$g tamoxifen (T-5648, Sigma) for five days to achieve lineage tracing of VSMCs. All mice were housed in a temperature-controlled environment maintained at 18–25 °C with a 12-h light/dark cycle. *Ldlr$^{-/-}$* and *B6G/R Myh11$^{Cre}$ Ldlr$^{-/-}$* mice were fed with a Clinton/Cybulsky High Fat Rodent Diet (HFD, 40% calories from fat; and 1.25% cholesterol, D12108C, Research Diets) for 12 or 24 weeks to induce atherosclerosis. Mice were sacrificed by cervical dislocation and then sequentially perfused with 5 mL of phosphate-buffered saline (PBS), followed by 10 mL of 4% paraformaldehyde, and finishing with another 5 mL of PBS, via the left ventricle. Mouse aortas, brachiocephalic arteries, and hearts were carefully dissected and embedded in the Optimal Cutting Temperature compound before being frozen, sectioned, and subjected to further analysis. The Animal Care and Use Committees of the Shanghai Tenth People's Hospital, affiliated with Tongji University, approved all animal studies in compliance with animal welfare regulations. All procedures were carried out per the "Guideline for the Care and Use of Laboratory Animals" published by the National Institutes of Health (NIH Publication, 8th Edition, 2011). Our animal ethics approval number is: SHDSYY-2022-2149.

*CCK-8 Test*: Cells were first incubated in a complete medium for 24 h in an incubator (37 °C, 5% $CO_2$) to ensure attachment. Subsequently, the cells were then incubated with SFGL. Afterwards, 10 µl of Cell Counting Kit 8 (k1018, APExBIO) solution was added to each well. The cells were protected from light and incubated for 2 h, and then the absorbance was measured at 450 nm.

*Flow Cytometry and Immunofluorescent Detection*: The efficiency of SFGL in targeting different cell types was determined by using flow cytometry-based Cy5 conjugated SFGL. The positive cells were analyzed using FlowJo Software (V10.0.7, USA). After the cells were seeded at $1 \times 10^5$ cells/well on culture dishes, we incubated them with different concentrations of Cy5 conjugated SFGL for 12 h. Then, we fixed the cells with 4% paraformaldehyde for 15 min, then permeabilized them with 0.2% Triton X-100 (X100RS, Sigma, USA) in PBS for 5 min. Nuclei were labeled with DAPI (Vector Laboratories), and fluorescently labeled cells were then visualized using an LSM710 laser confocal microscope (Carl Zeiss, Germany). Image J was used to calculate the area of the lesion area or the positive region.

*Fluorescence Imaging*: Fluorescence imaging of SFGL conjugated with FITC was performed with *Ldlr$^{-/-}$* mice. *Ldlr$^{-/-}$* mice were treated with an HFD for 24 weeks to establish an atherosclerotic model. 12 experimental mice were divided into 4 groups of three mice each: Each group was injected with SFGL conjugated with FITC. After that, 4 groups of mice were euthanized at different time points of 3, 6, 12, and 24 h. Postmortem, the aortas and other major organs from each mouse were obtained to evaluate the fluorescence activity of the nanoparticles. The fluorescence intensity of different nanoparticles was detected with the IVIS lumina small animal live imaging system (PerkinElmer, USA). Moreover, the relative fluorescence signal intensity was quantitatively analyzed using the Living Image software (4.4).

*NIR-II Imaging*: NIR-II imaging of SFGL conjugated with IR-1061 was performed with **Myh11$^{\text{Cre}}$ B6-G/R Ldlr$^{-/-}$ SMCs lineage-tracing mice**. NIR-II fluorescence images (1000 nm, 1000 LP, 0.05 W cm$^{-2}$, and 200 ms) were taken using a in vivo NIR-II fluorescence imaging system (Shanghai United Digital Biotech. Co. Ltd., NIR-II-ST) with a commercial InGaAs array detector (1000-1700 nm).

*Photoacoustic Imaging*: Photoacoustic imaging of SFGL conjugated with cy5 was performed with **Myh11$^{\text{Cre}}$ B6-G/R Ldlr$^{-/-}$ SMCs lineage-tracing mice**. The mice were anesthetized in the imaging chamber of photoacoustic imaging instrument (Vevo LAZR, FujiFilm VisualSonics Inc., USA). A 685 nm pulse laser was used for excitation.

*Atherosclerotic Lesion Analyses*: The right common carotid arteries and the aortic arch from the atherosclerotic mice were carefully excised and processed for histology. HE staining was performed for morphological analysis. The collagen contents at the injured or ruptured areas were quantified with Masson staining. All analyses were performed by Image J software (V2.10 NIH USA).

*Murine MI Model*: Mice were anesthetized with pentobarbital sodium (50 mg kg$^{-1}$, Intraperitoneal injection) and intubated with a 22-gauge incubation tube while being mechanically ventilated with a small rodent respirator. A left thoracotomy was performed between the third and fourth intercostal space. The left anterior descending coronary artery (LAD) segment corresponding to ≈1.5–2 mm below the tip of the left auricle was permanently ligated with an 8-0 monofilament nylon suture. Then, the chest wall was closed, and air in the thorax was evacuated. Mice in the sham group underwent the same procedure without LAD ligation. After surgery, cardiac function was examined by echocardiography. All mice were carefully monitored each day after MI. Mice that died immediately or had an ejection fraction (EF) > 50% after surgery were excluded from this study. Heart samples were harvested at different time points for subsequent experiments.

*Cell Culture and Stimulation*: Rat aortic smooth muscle cells (A7r5, RASMCs) were purchased from Shanghai Zhongqiaoxinzhou Biotechnology. Cells were cultured in DMEM (SH30243.01, HyClone) with 10% FBS (10099141, Gibco) and 1% penicillin-streptomycin at 37 °C with 5% $CO_2$. The A7r5 cells were stimulated with water-soluble cholesterol (10 µg mL$^{-1}$, 72 h, C4951-30MG, Sigma), FGF21 (5 ng mL$^{-1}$, 24 h, HY-P7173, MCE), ox-LDL (100 µg mL$^{-1}$, 24 h, P00794, Solarbio), palmitic acid (300 µmol L$^{-1}$, 12 h, HY-N0830, MCE), lactate (10 mM, 12 h, HY-B227, MCE), and oxyhemoglobin (20 µg mL$^{-1}$, 6 h, YO-7109, Bomei Biotech). After stimulations, the cells were harvested for downstream experiments.

*Real-Time Quantitative Polymerase Chain Reaction (RT-qPCR)*: Total RNA was extracted using Trizol regent (Thermo Fisher, USA) according to the manufacturer's instructions. Purified RNA (1000 ng) was reverse-transcribed using a Primer Script RT Reagent Kit (rr820a, Takara). The qPCR was then performed on the cDNA product using FastStart Universal SYBR Green Master (QR0100, Roche) on a Roche Light cycler. The primers were listed in Table S2 (Supporting Information).

*ScRNA-seq Data Processing*: The scRNA-seq data derived from tdTomato$^{+}$ cells and zsGreen$^{+}$ cells isolated from the aortas of HFD-fed *B6-G/R Myh11$^{Cre}$* mice (GSE197073) were generated in our previous study.[23] To analyse these datasets, we employed the widely used Seurat v3.1.1 in R.[37] As a crucial step, we conducted rigorous quality control to exclude cells with poor gene expression profiles. Specifically, we excluded cells that expressed fewer than 200 genes or those with more than 10% mitochondrial genes among the total expressed genes. After normalization, we performed Principal Components Analysis and calculated the number of significant principal components using the Elbow Plot function. For unsupervised clustering, we employed the UMAP algorithm, setting the resolution to 0.6 to ensure a better annotation of cell types. In addition, marker genes were defined based on the Find Marker function and literature.

*Micro-CT*: The samples were subjected to micro-CT scanning (vivaCT 80; SCANCO Medical AG, Switzerland) at 55 kV with a resolution of 9 µm after perfusion with PBS and contrast agent. Dragonfly software (Object Research Systems Inc, Canada) was used for data analysis and image processing.

*Statistical Analysis*: Statistical analysis was performed using GraphPad Prism (Version 9.0). Results were displayed as mean ± standard error of the mean (SEM). Student's *t*-test or Mann-Whitney *U*-test was used to analyze the difference between standard and non-normal variables. Differences across more than three groups were compared using one-way ANOVA followed by a post hoc analysis with the Bonferroni test. $p < 0.05$ was treated as statistical significance.

## Supporting Information

Supporting Information is available from the Wiley Online Library or from the author.

## Acknowledgements

M.Z., X.L., and Z.L. contributed equally to this work. The authors thank the National Key Research and Development Program of China (2023YFA0915300), Nos. 52125303, 82270473, 82200277, 82070230, 92356305, 22431002, and 82270867 from the Chinese National Natural Science Foundation, Grant No. SHDC22023223 from the Shanghai Hospital Development Center Foundation, and the Innovation Program of Shanghai Municipal Education Commission (2023ZKZD02) for financial support.

## Conflict of Interest

The authors declare no conflict of interest.

## Data Availability Statement

The data that support the findings of this study are available from the corresponding author upon reasonable request.

## Keywords

atherosclerosis, glycolipid, macrophage targeting, micro-CT, self-assembly

Received: June 24, 2025
Revised: August 10, 2025

---

[1] P. Libby, *Nature* **2021**, *592*, 524.
[2] J. Fan, T. Watanabe, *Pathol. Int.* **2022**, *72*, 151.
[3] J. Frostegård, *BMC Med.* **2013**, *11*, 117.
[4] G. Mendieta, S. Pocock, V. Mass, A. Moreno, R. Owen, I. García-Lunar, B. López-Melgar, J. J. Fuster, V. Andres, C. Pérez-Herreras, H. Bueno, A. Fernández-Ortiz, J. Sanchez-Gonzalez, A. García-Alvarez, B. Ibáñez, V. Fuster, *J. Am. Coll. Cardiol.* **2023**, *82*, 2069.
[5] L. Fernández-Friera, J. L. Peñalvo, A. Fernández-Ortiz, B. Ibañez, B. López-Melgar, M. Laclaustra, B. Oliva, A. Mocoroa, J. Mendiguren, V. Martínez de Vega, L. García, J. Molina, J. Sánchez-González, G. Guzmán, J. C. Alonso-Farto, E. Guallar, F. Civeira, H. Sillesen, S. Pocock, J. M. Ordovás, G. Sanz, L. J. Jiménez-Borreguero, V. Fuster, *Circulation* **2015**, *131*, 2104.
[6] L. Fernández-Friera, V. Fuster, B. López-Melgar, B. Oliva, J. M. García-Ruiz, J. Mendiguren, H. Bueno, S. Pocock, B. Ibáñez, A. Fernández-Ortiz, J. Sanz, *J. Am Coll. Cardiol.* **2017**, *70*, 2979.
[7] W. Brinjikji, J. Huston III, A. A. Rabinstein, G. M. Kim, A. Lerman, G. Lanzino, *J. Neurosurg.* **2016**, *124*, 27.
[8] E. Falk, *J. Am. Coll. Cardiol.* **2006**, *47*, C7.
[9] E. Gusev, A. Sarapultsev, *Int. J. Mol. Sci.* **2023**, *24*, 7910.
[10] Z. Qian, Y. Zhao, C. Wan, Y. Deng, Y. Zhuang, Y. Xu, Y. Zhu, S. Lu, Z. Bao, *Front. Pharmacol.* **2021**, *12*, 652963.
[11] A. Zernecke, F. Erhard, T. Weinberger, C. Schulz, K. Ley, A. E. Saliba, C. Cochain, *Cardiovasc. Res.* **2023**, *119*, 1676.
[12] Y. V. Bobryshev, N. G. Nikiforov, N. V. Elizova, A. N. Orekhov, *Results Probl. Cell. Differ.* **2017**, *62*, 273.
[13] P. Swiatlowska, W. Tipping, E. Marhuenda, P. Severi, V. Fomin, Z. Yang, Q. Xiao, D. Graham, C. Shanahan, T. Iskratsch, *Adv. Sci. (Weinh)* **2024**, *11*, 2308686.
[14] F. Burger, D. Baptista, A. Roth, R. F. da Silva, F. Montecucco, F. Mach, K. J. Brandt, K. Miteva, *Int. J. Mol. Sci.* **2021**, *23*, 340.
[15] Y. Bao, L. Zhu, Y. Wang, J. Liu, Z. Liu, Z. Li, A. Zhou, H. Wu, *Phytomedicine* **2024**, *128*, 155341.
[16] P. M. Ridker, B. M. Everett, T. Thuren, J. G. MacFadyen, W. H. Chang, C. Ballantyne, F. Fonseca, J. Nicolau, W. Koenig, S. D. Anker, J. J. P. Kastelein, J. H. Cornel, P. Pais, D. Pella, J. Genest, R. Cifkova, A. Lorenzatti, T. Forster, Z. Kobalava, L. Vida-Simiti, M. Flather, H. Shimokawa, H. Ogawa, M. Dellborg, P. R. F. Rossi, R. P. T. Troquay, P. Libby, R. J. Glynn, *N. Engl. J. Med.* **2017**, *377*, 1119.
[17] M. R. Bennett, S. Sinha, G. K. Owens, *Circ. Res.* **2016**, *118*, 692.
[18] L. Gatto, G. Paoletti, V. Marco, A. La Manna, F. Fabbiocchi, B. Cortese, R. Vergallo, A. Boi, M. Fineschi, A. Di Giorgio, N. Taglieri, G. Calligaris, S. Budassi, F. Burzotta, F. Isidori, E. Lella, G. Ruscica, M. Albertucci, C. Tamburino, Y. Ozaki, F. Alfonso, E. Arbustini, F. Prati, *Int. J. Cardiovasc. Imaging* **2021**, *37*, 37.
[19] P. Schoenhagen, S. E. Nissen, *Am Heart Hosp. J.* **2003**, *1*, 164.
[20] A. J. V. Mézquita, F. Biavati, V. Falk, H. Alkadhi, R. Hajhosseiny, P. Maurovich-Horvat, R. Manka, S. Kozerke, M. Stuber, T. Derlin, K. M. Channon, I. Išgum, A. Coenen, B. Foellmer, D. Dey, R. Volleberg, F. G. Meinel, M. R. Dweck, J. J. Piek, T. van de Hoef, U. Landmesser, G. Guagliumi, A. A. Giannopoulos, R. M. Botnar, R. Khamis, M. C. Williams, D. E. Newby, M. Dewey, *Nat. Rev. Cardiol.* **2023**, *20*, 696.
[21] H. Kosuge, M. Nakamura, A. Oyane, K. Tajiri, N. Murakoshi, S. Sakai, A. Sato, A. Taninaka, T. Chikamori, H. Shigekawa, K. Aonuma, *Mol. Imaging Biol.* **2022**, *24*, 692.
[22] J. Qin, C. Peng, B. Zhao, K. Ye, F. Yuan, Z. Peng, X. Yang, L. Huang, M. Jiang, Q. Zhao, G. Tang, X. Lu, *Int. J. Nanomed.* **2014**, *9*, 5575.
[23] M. Zhai, S. Gong, P. Luan, Y. Shi, W. Kou, Y. Zeng, J. Shi, G. Yu, J. Hou, Q. Yu, W. Jian, J. Zhuang, M. W. Feinberg, W. Peng, *Nat. Commun.* **2022**, *13*, 7500.
[24] M. P. de Winther, K. W. van Dijk, L. M. Havekes, M. H. Hofker, *Arterioscler. Thromb. Vasc. Biol.* **2000**, *20*, 290.
[25] F. Moheimani, J. T. Tan, B. E. Brown, A. K. Heather, D. M. van Reyk, M. J. Davies, *Exp. Diabetes Res* **2011**, *2011*, 1.
[26] M. Shi, C. Wang, H. Mei, M. Temprosa, J. C. Florez, M. Tripputi, J. Merino, L. Lipworth, X. O. Shu, R. E. Gerszten, T. J. Wang, J. A.

Beckman, J. L. Gamboa, J. D. Mosley, J. F. Ferguson, *J. Am Heart. Assoc.* **2022**, *11*, 024388.

[27] L. Chollet, P. Saboural, C. Chauvierre, J.-N. Villemin, D. Letourneur, F. Chaubet, *Marine Drugs* **2016**, *14*, 145.

[28] Z. Lin, X. Tan, Y. Zhang, F. Li, P. Luo, H. Liu, *Marine Drugs* **2020**, *18*, 376.

[29] K. Xiao, Y. Li, J. Luo, J. S. Lee, W. Xiao, A. M. Gonik, R. G. Agarwal, K. S. Lam, *Biomaterials* **2011**, *32*, 3435.

[30] L. Zhang, X. Y. Tian, C. K. W. Chan, Q. Bai, C. K. Cheng, F. M. Chen, M. S. H. Cheung, B. Yin, H. Yang, W. Y. Yung, Z. Chen, F. Ding, K. C. Leung, C. Zhang, Y. Huang, J. Y. W. Lau, C. H. J. Choi, *ACS Appl. Mater. Interfaces* **2019**, *11*, 13888.

[31] M. Nahrendorf, H. Zhang, S. Hembrador, P. Panizzi, D. E. Sosnovik, E. Aikawa, P. Libby, F. K. Swirski, R. Weissleder, *Circulation* **2008**, *117*, 379.

[32] Q. Bai, Y. Xiao, H. Hong, X. Cao, L. Zhang, R. Han, L. K. C. Lee, E. Y. Xue, X. Y. Tian, C. H. J. Choi, *Proc. Natl. Acad. Sci. U S A* **2022**, *119*, 2201443119.

[33] E. J. Chung, M. Tirrell, *Adv. Healthcare Mater.* **2015**, *4*, 2408.

[34] C. Tu, T. S. C. Ng, H. K. Sohi, H. A. Palko, A. House, R. E. Jacobs, A. Y. Louie, *Biomaterials* **2011**, *32*, 7209.

[35] L. W. C. Ho, W.-Y. Yung, K. H. S. Sy, H. Y. Li, C. K. K. Choi, K. C. Leung, T. W. Y. Lee, C. H. J. Choi, *ACS Nano* **2017**, *11*, 6085.

[36] H. Wang, L. Yao, X. Mao, K. Wang, L. Zhu, J. Zhu, *Nanoscale* **2019**, *11*, 13917.

[37] R. Satija, J. A. Farrell, D. Gennert, A. F. Schier, A. Regev, *Nat. Biotechnol.* **2015**, *33*, 495.